Effect of Powder Shape and Size on Rheological, Thermal, and Segregation Properties of Low-Pressure Powder Injection Molding Feedstocks

Mohamed Aziz Ben Trad, Vincent Demers, and Louis Dufresne

Optimization of molding parameters at different filling stages requires that the characteristics of low-viscosity feedstocks must be properly known. In this study, the influence of the particle size (3, 7, and 12 µm) and powder morphology (gas- and water-atomized) was quantified using different feedstock formulations based on a 17-4 PH stainless steel powder, all combined with the same binder system. The specific heat capacity, viscosity, and segregation levels were assessed using a differential scanning calorimeter, a rotational rheometer, and a thermogravimetric analyzer, respectively. It was then shown that the feedstock prepared with the gas-atomized powder exhibits a higher specific heat capacity value when compared to a water-atomized powder (i.e., Cp varying from 0.6 to 0.3 J/g K, respectively). It was also shown that the feedstock viscosity profiles and the intensity of segregation both depend significantly on the powder shape and size used in the feedstock formulation. For short processing times (e.g., < 1 min spent in molten state), a feedstock formulated with coarse gas-atomized powder can be considered to be the best candidate for an injection process because its viscosity and segregation potential are relatively low (with a viscosity varying from 0.5 to 2 Pa s, and a volume fraction of powder close to 60 vol.%). Following this, the moldability index was used to predict that coarser water-atomized powder (i.e., 12 versus 7 µm) will not have a significant effect on the molding properties, and can be seen as a potential means of decreasing shrinkage during sintering without impacting the injection properties. For very long processing times, the magnitude of segregation remains insignificant for feedstock formulated with fine powder (i.e., a volume fraction of powder remaining close to 60 vol.%). However, this important gain (i.e., no segregation) comes with a significant increase in viscosity varying from 2 to 10 Pa s, resulting in a decrease in the molding properties.

1. Introduction

Metal injection molding (MIM) is a well-adapted process for the manufacture of small, precise, and complex shape metallic parts with high service properties and produced at low cost. The MIM process involves feedstock preparation by mixing a metallic powder with a molten binder, which is injected into a mold cavity to form the required shape after solidification of the binder. This green part is then debound and sintered to completely remove the binder and obtain a near-net-shaped dense metallic component (Ref 1-3). Recently, the high-viscosity feedstocks used in the conventional high-pressure powder injection molding process (HPIM, using an injection pressure varying from 50 to 200 MPa) have been modified to design new low-viscosity feedstocks adapted for the low-pressure powder injection molding process (LPIM). These wax-based feedstocks are generally characterized by a low melting

point (e.g., < 120°C) and low viscosity (e.g., < 10 Pa s), leading to injections performed at pressures generally lower than 1 MPa (Ref 4, 5). Initially developed for the production of ceramic components, the LPIM process has been adapted for the fabrication of metallic parts in the aerospace and medical industries (Ref 6, 7).

The rheological behavior of the feedstock is a key parameter used to control the mold filling operation during injection. Mangel et al. (Ref 8) were the pioneers in this regard, and used the spiral flow distance to demonstrate that the moldability of LPIM feedstocks is inversely proportional to its viscosity. It is well-known that powder characteristics influence the flow behavior of feedstocks. In general, the viscosity decreases with an increase in the particle sphericity, an increase in particle size, and a decrease in particle surface roughness. For example, Jamaludin et al. (Ref 9) used coarse and fine powder lots to formulate HPIM feedstocks and quantify that a decrease in powder size from 15 to 7 µm almost doubles the viscosity values. Heaney et al. (Ref 10) confirmed that agglomerations present in water-atomized powders were responsible to the dimensional variability of HPIM components. Contreras et al. (Ref 11) used fine bronze powders (9-13 µm) to demonstrate the higher solid loading obtained with spherical shape (i.e., 70-73 vol.% of powder) compared to irregular shape (63-65 vol.% of powder). Water and gas atomization are two techniques that are widely used to produce irregular and spherical particles that are utilized in HPIM and LPIM metallic-based feedstocks. It is generally well-accepted that feedstocks formulated from a gas-atomized powder provide a better injection molding capability,

Mohamed Aziz Ben Trad, Vincent Demers, and Louis Dufresne, École de technologie supérieure (U. Quebec), 1100 Notre-Dame West, Montreal, QC H3C 1K3, Canada. Contact e-mails: mohamed-aziz. ben-trad.1@ens.etsmtl.ca, vincent.demers@etsmtl.ca, and louis. dufresne@etsmtl.ca.

but are generally more expensive than those formulated from water-atomized powder. This moldability improvement is generally related to a decrease in interparticle friction combined with a decrease in energy required for the powder orientation with the flow during an injection. For LPIM feedstocks, the effect of the powder shape and size on the rheological behavior has mainly been studied for ceramic-based powder–binder mixtures. Hausnerova et al. (Ref 12) confirmed that the flow properties of carbide-based feedstocks are influenced by the size and particle size distribution of a powder, where the mixtures formulated with the powders having a high portion of small particles tend to have high viscoelastic function. Schlechtriemen et al. (Ref 13) used two similar ceramic mixtures with different specific surfaces and morphology to tailor the powder characteristics providing suitable feedstock properties for low-pressure injection molding process.

The thermal properties of feedstocks are also crucial in setting the injection parameters and establishing the constitutive equations required to numerically simulate the injection step. Calorimetric analysis is routinely used in HPIM and in LPIM to measure the melting point of feedstock. This test is well-adapted to study the interaction between the binder constituents and to properly set the minimum injection temperature (Ref 14-17). This technique is also somewhat used in HPIM to evaluate the specific heat capacity of different powder–binder mixtures and predict the solidification behavior during cooling of the component (Ref 18). As validated by Chung et al. (Ref 19), the heat capacity of a given feedstock can easily be approximated by a rule of mixture using the heat capacities and weight fractions of each constituent, but this technique has thus far only been validated for a few HPIM feedstocks (Ref 9, 20-23). For LPIM mixtures, the effect of the powder shape and size on the specific heat capacity has received very little attention in the literature.

Segregation is an undesirable effect which refers to a fluctuation in solid loading within the feedstock (i.e., before or after injection), and which must be minimized to prevent distortions, cracks, warping, and heterogeneous shrinkage during the sintering step of the process. This inhomogeneous distribution of powder particles in the feedstock is generated by an improper mixing method during feedstock preparation, high shear deformation rate gradients during the molding process, or by the gravity of feedstock that remains idle during the process dead times (Ref 24-27). The segregation phenomenon occurring during the injection stage of HPIM or micro-PIM injections has been well-studied using different numerical approaches to investigate the role of injection parameters and predict the segregation effect through an injected part. Gelin et al. (Ref 28) developed a biphasic simulation approach to assess the variation of powder volume fraction at different filling stages of the process and predicted the segregation effect through an injected part. Similar models were used by Fang et al. (Ref 29) to investigate the influence of filling patterns on the powder–binder separation after molding. Hao et al. (Ref 30) used a granular model to predict the evolution of the density through a triangular mold due to the segregation effect. The role of injection parameters, the location, and the intensity of segregation during injection were also studied using commercial and in development software (Ref 31). Recent studies on the segregation effects of LPIM-molded parts have focused mainly on the development of experimental techniques to investigate the role of injection parameters or feedstock attributes in segregation. Hausnerova et al. developed an experimental technique based on SEM/EDX to detect powder–binder separation (Ref 32, 33). Demers et al. used the TGA technique to measure a nonuniform distribution of powder particles through rectangular and wedge-shaped molded parts processed by LPIM (Ref 34). Poh et al. demonstrated the strength of this TGA technique in the development of ceramic-based LPIM mixtures (Ref 35). Shivashankar et al. used a capillary rheometer to investigate the segregation of low and moderate viscosity mixtures, while Mukund et al. combined capillary rheology and density measurements to quantify the powder–binder separation in moderate pressure powder injection molding process feedstocks (Ref 36, 37). During injection dead times, segregation generated by gravity may occur for feedstocks that remain idle (e.g., that are trapped in the injection press), producing a powder–binder mixture that could be inappropriate for further injections. This type of segregation has only been superficially examined in a conventional HPIM due to the inherently high-viscosity feedstocks, which prevent the occurrence of this phenomenon. For LPIM feedstocks, an experimental model was developed and recently refined to highlight that the segregation of unmixed feedstocks depends on the binder constituents and idle time (Ref 34). Although the influence of powder shape and size on rheological properties at high shear rate for 17-4PH-based feedstocks was evaluated by Hausnerova et al. (Ref 5), the characterization of the feedstock viscosity experienced in LPIM process (i.e., at shear rate lower than 100 s^{-1}) remains a challenge. In addition, the influence of powder characteristics on thermal and segregation properties is still in infancy. The aim of this study is to investigate the effect of the powder shape and size on the rheological behavior, thermal properties, and segregation of metal-based LPIM feedstocks.

2. Material and Measurements

2.1 Powder Characteristics and Feedstock Preparation

Four different powder lots were used in this study (Table 1). Three water-atomized stainless steel 17-4PH powders (Epson Atmix Corporation, Japan), with a typical near-spherical or ligament shape and nominal particle sizes of 3, 7, and 12 μm (Fig. 2a-c), and one gas-atomized stainless steel 17-4PH powder (Sandvik Osprey Ltd, United Kingdom), with a spherical shape and a nominal particle size of 12 μm (Fig. 2d) were used. This precipitation-hardening stainless steel is widely used in the aerospace, chemical, petrochemical, and many other sectors for its high strength and good corrosion resistance.

Each powder lot presented in Table 1 was combined with molten binder (90°C) in a laboratory mixer and blended for 45 min under vacuum. The solid loading was set at 60 vol.% of powder to prepare four different feedstocks using the same low melting point binder system formulated from 30 vol.% of paraffin wax (PW), 7 vol.% of carnauba wax (CW), 2 vol.% of stearic acid (SA), and 1 vol.% of ethylene vinyl acetate (EVA). This solid loading represents a typical value for obtaining homogeneous powder–binder mixtures. These binder constituents were selected due to their extensive use in LPIM, to help with the part ejection after mold filling (i.e., PW and CW), to promote the surfactant effect enhancing chemical links between the powder and binder (i.e., SA), and to produce the thickening effect needed to control the segregation of powder

Table 1 17-4PH powder characteristics

Powder lot	Atomization technique	Density, g cm^{-3}	d_{10}, μm	d_{50}, μm	d_{90}, μm	Specific surface area, m^2 g^{-1}	Supplier
PF-3K	Water	7.8	1.2	2.7	5.4	0.30	Atmix
PF-13F	Water	7.8	2.3	7.0	20.3	0.10	Atmix
PF-20F	Water	7.8	3.4	11.8	31.3	0.08	Atmix
S17700	Gas	7.8	3.0	11.3	27.5	0.09	Osprey

Table 2 Volume fraction of powder and binder used for feedstock formulations

		Vol.%							
		Powder				Binder			
Feedstock formulation	Melting point, °C	PF-3K	PF-13F	PF-20F	S17700	PW	CW	SA	EVA
3-W	77.5	60	...	...	...	30	7	2	1
7-W	77.5	...	60	...	...	30	7	2	1
12-W	77.5	...	...	60	...	30	7	2	1
12-G	77.5	...	...	...	60	30	7	2	1

(i.e., EVA) (Ref 38-40). It should be noted that this binder formulation does not contain one backbone polymer (i.e., the constituent often used in high-pressure powder injection molding process feedstocks to maintain the shape up to the pre-sintering state). Therefore, all binders could be removed in just one step using wicking debinding where the green parts are embedded into a wicking powder bed (e.g., alumina, graphite, silica clay, zirconia, or other inert powder) before being thermally debounded under protective atmosphere (not performed in this study). The role of the wicking media is to withdraw the liquid binder by capillary force (i.e., the carrier binder, the surfactant, and the thickening agent at the same time), as well as to maintain the shape up to the pre-sintering of powder particles. Feedstock formulations presented in Table 2 are referenced by their nominal powder sizes (i.e., 3, 7, or 12 μm) and atomization techniques (i.e., W for water or G for gas). For example, the feedstock 3-W is a mixture containing 60 vol.% of 3 μm water-atomized powder with 30 vol.% of PW, 7 vol.% of CW, 2 vol.% of SA, and 1 vol.% of EVA.

2.2 Measurement

The particles' size distribution and specific surface areas were measured using an LS 13320 Beckman Coulter laser diffraction particle analyzer. A scanning electron microscope (Hitachi 3600) was used to qualitatively evaluate the particle shape of each dry powder lot and to examine the segregated state of feedstocks using a secondary electrons detector (under a high vacuum) and a back-scattered electrons detector (under partial pressure), respectively. Thermal properties were obtained with a PerkinElmer Pyris 1 differential scanning calorimeter (DSC). The melting point and specific heat of feedstocks were measured according to ASTM D3418 and ASTM E1269, respectively (Ref 41, 42). Feedstock and single-binder specimens with a mass ranging from 8 to 12 mg were encapsulated in standard aluminum hermetic pans and tested over temperatures ranging from 20 to 120°C (heating rate of 10°C min^{-1}) under dry nitrogen gas flow (50 ml min^{-1}). The DSC thermograms were recorded from the second heating

Table 3 Melting points, density, and decomposition temperature of the binders

Binders	Melting point, °C	Density, g cm^{-3}	Decomposition temperature, °C
PW	59.0	0.9	...
CW	84.5	1.0	310
EVA	49.0	1.0	400
SA	75.0	0.9	520

cycle to minimize the thermal history and maximize the thermal contact between the pan and specimen. The melting points of each single binder are reported in Table 3. DSC curves required to calculate the specific heat of the feedstocks (i.e., thermograms for the specific heat capacity of the specimen holder and sapphire standard) were repeated twice.

The specific heat capacities of feedstocks were calculated from Eq 1 using the DSC thermograms obtained with feedstocks, a standard material, and an empty pan.

$$Cp_{(\text{feedstock})} = Cp_{(\text{standard})} \cdot \frac{D_1 \cdot W_{\text{standard}}}{D_2 \cdot W_{\text{feedstock}}} \quad \text{(Eq 1)}$$

where $Cp_{(\text{feedstock})}$ is the specific heat capacity of the feedstock, $Cp_{(\text{standard})}$ is the specific heat capacity of the standard material (i.e., sapphire), D_1 is the heat flow difference (in W g^{-1}) between the DSC profiles obtained with the empty pan and feedstock, D_2 is the heat flow difference (in W g^{-1}) between the DSC profiles obtained with the empty pan and the standard material, $W_{\text{feedstock}}$ is the mass of feedstock, and W_{standard} is the mass of the standard material (Ref 42).

The rheological behavior of the feedstocks was characterized using an Anton Paar MCR 302 rotational rheometer with a CC-17 concentric cylinders and a C-PTD 200 Peltier temperature-controlled measuring system. Molten feedstocks were poured into the cylinder, and then tested at shear deformation rates ranging from 0.5 to 3500 s^{-1} at three different temper-

atures (80, 90, and 100°C). Each testing condition was repeated three times with different molten samples. The moldability of the feedstock was calculated using the moldability index model according to Eq 2

$$\alpha_{stv} = \frac{10^6}{\eta_0} \cdot \frac{|n-1|}{E/R} \qquad \text{(Eq 2)}$$

where α_{stv} is the moldability index, η_0 is the viscosity at a reference shear rate representing the molding process (viscosity at $100 \ s^{-1}$ in this project), n is the flow behavior index, E is the activation energy for viscous flow, and R is the gas constant. This simple model was initially developed to compare the molding performance of plastic (Ref 43), and was recently introduced in HPIM and LPIM to assess the molding potential of feedstocks (Ref 44-46).

The segregation potential of the feedstocks was characterized using a PerkinElmer Diamond TG/DTA thermogravimetric analyzer (TGA) according to the method developed in (Ref 47), and recently refined in (Ref 34). Each feedstock was poured into cylindrical hot molds (Fig. 1a), maintained at 90°C for three different time periods (1, 10, and 60 min), and rapidly cooled to room temperature to form a cylindrical green part (Fig. 1b). Cubic specimens of about 1 mm³ were then extracted from three different positions of the molded part (i.e., from the top, the middle, and the bottom of the molded part) according to the pattern shown in Fig. 1(c). The specimens were placed in standard platinum pans and then heated from 20 to 800°C (heating rate of 20°C min⁻¹) under high-purity nitrogen purge gas (flow rate of 60 ml min⁻¹). The solid loading over the molded part was calculated from the TGA profiles according to the weight fraction of the remaining powder after binder burnout at these three different positions within the molded specimens according to Eq 3.

3. Results and Discussion

3.1 Powder Size and Morphology

Figure 2(a)-(d) presents the morphology of the powder lots produced by water atomization and gas atomization. Although all these powder lots exhibit a high degree of sphericity, the water atomization technique produces significantly more non-spherical powders characterized by irregular, ligamental, or ellipsoidal shapes as indicated by the white arrows in Fig. 2. Frequency curves and cumulative particle size distributions are plotted in Fig. 2(e)-(h) to assess the relative amount of particles constituting each powder lot and to quantify typical powder characteristics such as d_{10}, d_{50}, d_{90}, and the specific surface area, all reported in Table 1. In general, particle-to-particle contacts per unit of volume in a feedstock increase as the particle size decreases. Therefore, the energy dissipated under the form of interparticular friction leads in an increase in feedstock viscosity (clearly visible with the feedstock 3-W in Fig. 5 due to its low D_{50} value shown in Fig. 2e). In addition, it is well-accepted that bimodal particle size distribution leads to a higher packing compared to monomodal distribution, where solid loading as high as 70 and 73 vol.% was obtained for bimodal (and also trimodal) iron-based and bimodal Inconel-based feedstocks (Ref 48-50). In this respect, the optimal solid loading of the feedstocks 7-W, 12-W, and 12-G (not quantified in this study) is expected to be high due to their bimodal size distributions (Fig. 2f-h). Higher powder content into the binder is of practical interest to reduce the shrinkage and distortion during the sintering stage.

3.2 Differential Scanning Calorimetry Analyses

The differential scanning calorimetry profiles for single constituent and different feedstocks are presented in Fig. 3. The DSC curves exhibit several peaks corresponding to the different melting points of the binder, the feedstock melting point was determined from the last peak obtained during a heating cycle as indicated by a black arrow in Fig. 3. The melting points of the feedstocks were extracted from DSC thermograms, reported in Table 2, and finally used to set the minimum temperature for the rheological tests at 80°C (i.e., at slightly higher than the melting point) to guarantee the molten state of the feedstocks). A comparison of melting points obtained with single-binder and multiple constituents shown in Fig. 3 and also reported in Tables 2 and 3 confirms that the constituents have a certain
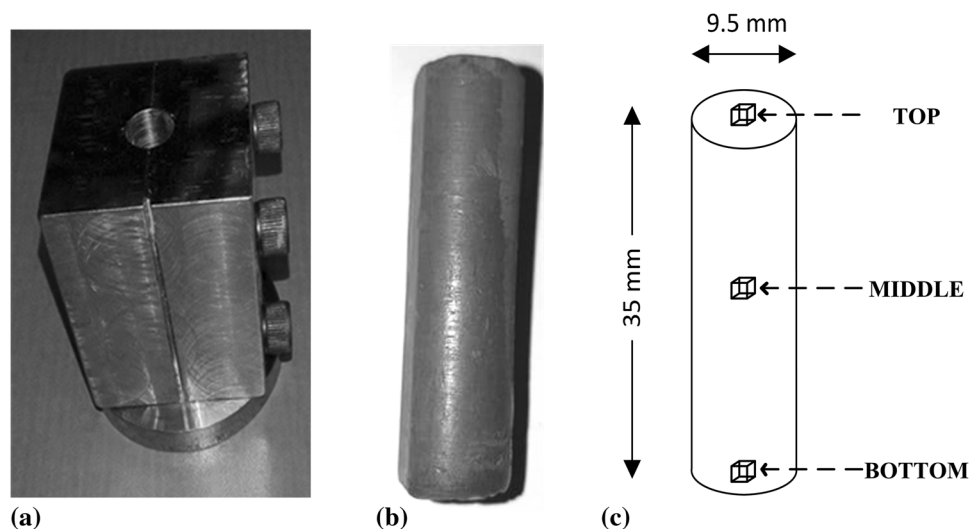

Fig. 1 Specimen preparation for segregation tests: (a) mold for the cylindrical part, (b) typical cylindrical green part, and (c) position of the extracted specimens within the cylindrical green part for TGA tests
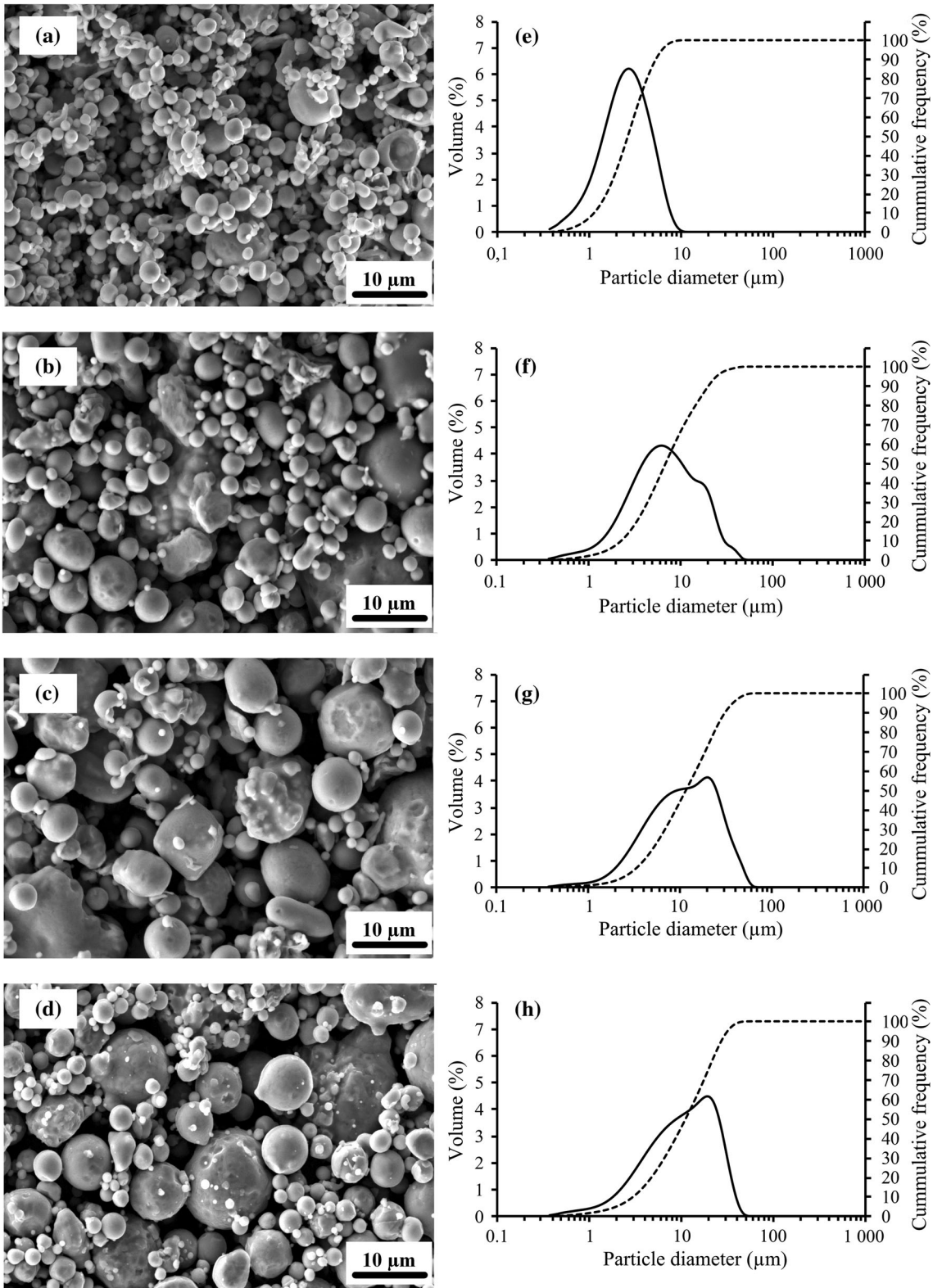
Fig. 2 SEM photographs and particle size distribution of different 17-4PH stainless steel powder lots (white arrows indicate non-spherical powders), (a and e) water-atomized D_{50} = 3 μm, (b and f) water-atomized D_{50} = 7 μm, (c and g) water-atomized D_{50} = 12 μm, and (d and h) gas-atomized D_{50} = 12 μm

degree of solubility together. Indeed, the mixture of carnauba wax with the other binder constituents generates a decrease in the melting point compared to the pure components (i.e., from 84.5°C for Carnauba wax versus 77.5°C for feedstock).

DSC thermograms were used to measure the values of the specific heat capacity (Cp), which are reported in Fig. 4 for each feedstock. The values of the specific heat capacity of an injected feedstock present the quantity of heat added to or
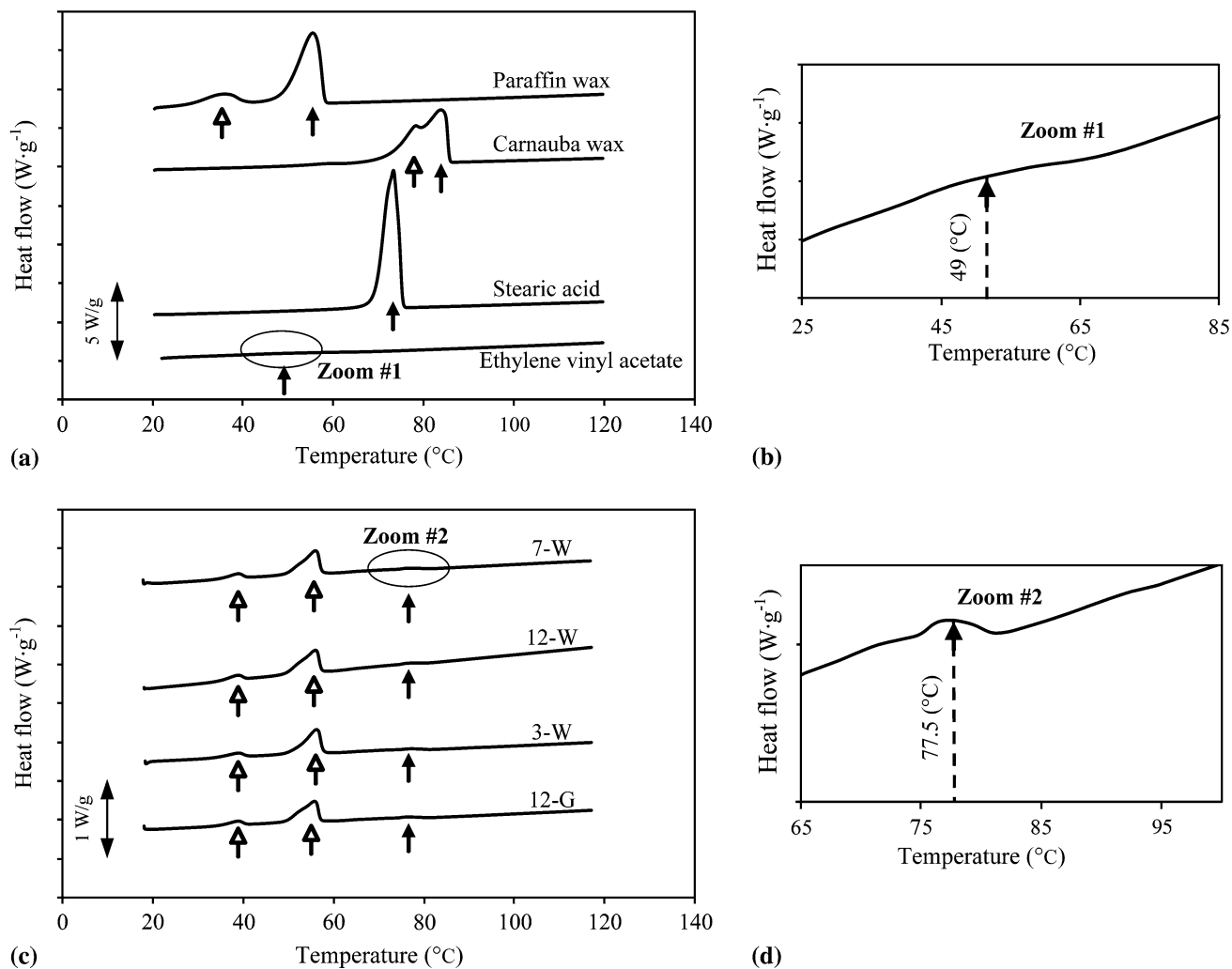
Fig. 3 DSC results for (a) single-binder constituent, (b) zoom for identification of EVA melting point, (c) all feedstocks, and (d) zoom for identification of feedstocks melting point
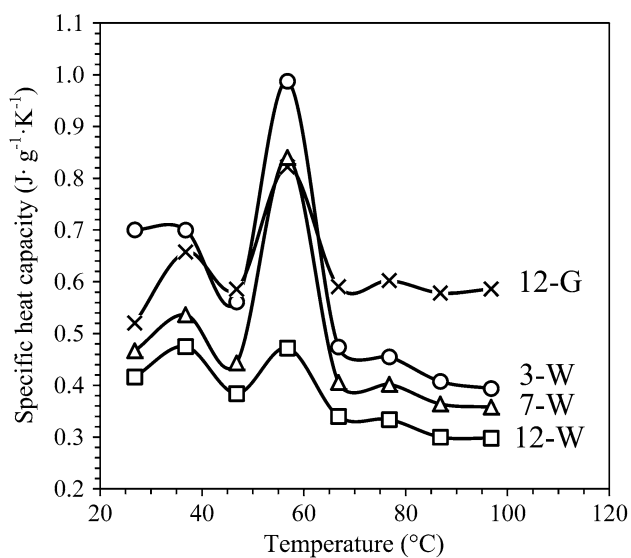

Fig. 4 Specific heat capacity of feedstocks according to temperature

removed from the feedstock required to change the temperature during mold filling and solidification of the component. It is well-accepted that the specific heat capacity can be estimated using a rule of mixture. This technique is widely used in composites to determine the Cp of a given composite material from the weight fraction and tabulated Cp of each constituent. Using this approach, the specific heat values are expected to be similar for all feedstocks used in this study since they were formulated using the same constituents (i.e., irrespective of the powder shape and size). However, for a given particle shape (e.g., water-atomized powder), the specific heat capacity of feedstock seems to increase with a decrease in particle size, with the feedstock 3-W generating a higher Cp value as compared to feedstock 12-W (Fig. 4). In this respect, the 7-W mixture exhibits a specific heat capacity value between those obtained with the feedstocks 3-W and 12-W. For the same particle size (i.e., $d_{50} = 12$ μm), the feedstock produced with the gas-atomized technique (feedstock 12-G) seems to demonstrate a higher specific heat capacity value than that produced with the water-atomized technique (feedstock 12-W), particularly in the liquid state (i.e., for the Cp values obtained at temperatures higher than 77.5°C in Fig. 4). A possible

explanation for this variation of the Cp for different powder characteristics would be that the contact surface condition between the powder and the binder can influence the heat capacity of a biphasic. Since trapped air could affect the thermal behavior of the feedstocks, pycnometer measurements check have shown values of a green density at 5.05 g/cm^3 representing the theoretical density of mixtures. The specific heat capacity measurement has received very little attention in the literature, and this impact of the particle size and the atomization technique must be confirmed in future works using, for example, the image analysis technique combined with a precise measurement of the specific surface using the physical adsorption of a gas approach (i.e., Brunauer–Emmett–Teller theory). Variation of the Cp for different powder characteristics is of practical importance in predicting the feedstock behavior during and after the injection stage.

3.3 Rheological Behavior of Feedstocks

The rheological behavior obtained at three different temperatures is shown in Fig. 5. All feedstocks are characterized by a near-Newtonian plateau observed at low shear rate (i.e., between 0.5 and 2 s^{-1}), followed by a clear and pronounced shear thinning behavior, where the viscosity decreases as the shear rate increases (i.e., between 2 and 3500 s^{-1}). At low shear rate, several feedstocks are characterized by a slight decrease in viscosity as the shear rate increases from 0. 5 to 0.9 s^{-1}, followed by a slight increase in viscosity as the shear rate increases from 0.9 to 2 s^{-1} (represented by a black arrow). Hausnerova et al. reported that this change from pseudoplastic to dilatant behavior at low shear rate can be explained by the difficulty to form particle layers, which in turn results in particles sliding over each other and resulting in an increase in viscosity (Ref 15, 51). This "hook" phenomenon was observed for all temperatures used in this study. The second pseudoplastic behavior (i.e., the one observed from 2 to 3500 s^{-1} for all feedstocks) was explained by a restructuring of the mixture, with the alignment of polymer chains and particles as the shear rate increased. During the injection step of the LPIM process, this latter pseudoplastic behavior is generally suitable for promoting the mold filling. Figure 5 also indicates that the viscosity values of LPIM feedstocks depend on the temperature, powder size, and powder shape. The lowest viscosity value was obtained with feedstock 12-G, while the highest was achieved with feedstock 3-W. A high particle surface area measured with feedstock 3-W (reported in Table 1) is certainly linked to an amplification of the friction forces between the powder and binder leading to an increase in viscosity as compared to the other feedstocks. In the same vein, similar particle surface area values (varying between 0.08 and 0.10 m^2 g^{-1}) measured for the other three feedstocks also are in phase with the similar viscosity values obtained with these feedstocks. For the same powder size (i.e., 12-W versus 12-G), the decrease in viscosity measured with feedstock 12-G may be attributable to a lower occurrence of irregularly shaped powder generally inherent to the gas atomization process.

Rheological parameters such as the reference viscosity (η_0), activation energy for flow (E), and shear sensitivity index (n) are extracted from Fig. 5 using the same methodology detailed in (Ref 52), and then plotted in Fig. 6. In this context, the degree of temperature sensitivity to viscosity change was captured with the value of E, while the degree of shear rate sensitivity to viscosity change was quantified with
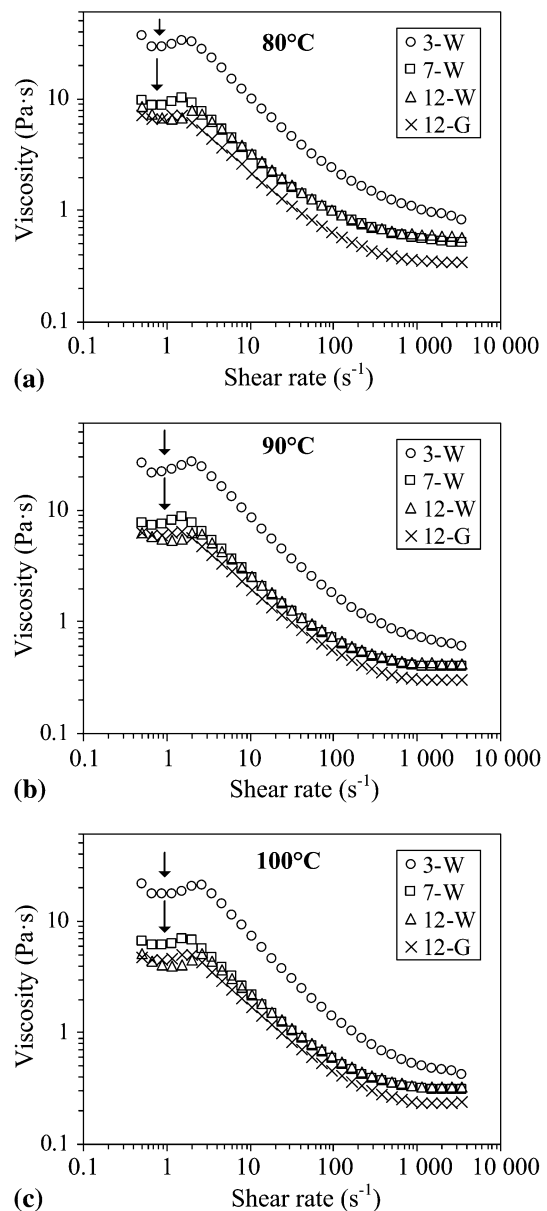

Fig. 5 Viscosity profiles for 3-W, 7-W, 12-W, and 12-G feedstocks at (a) 80, (b) 90, and (c) 100°C

the value of n. Although a viscosity change is expected with a change in temperature, a low value of E is suitable for minimizing sudden changes in feedstock viscosity between the hot and cold zones in the injection press or in the mold in order to minimize excessive residual stresses in green parts. For water-atomized feedstocks, the activation energy value decreases as the particle size increases. For the same powder size (i.e., 12-W versus 12-G), the significant decrease in temperature sensitivity measured with feedstock 12-G may also be attributable to the lower interparticle contacts for particles exhibiting higher sphericity. As reported above, all feedstocks are characterized by a value of $n < 1$, indicating that the feedstock viscosity is strongly dependent on the shear rate. Generally, the value of this shear rate sensitivity index should be as small as possible to maximize the viscosity changes during and after the mold filling. The mixture, 3-W, has the smallest value of n, while the three other mixtures (7-
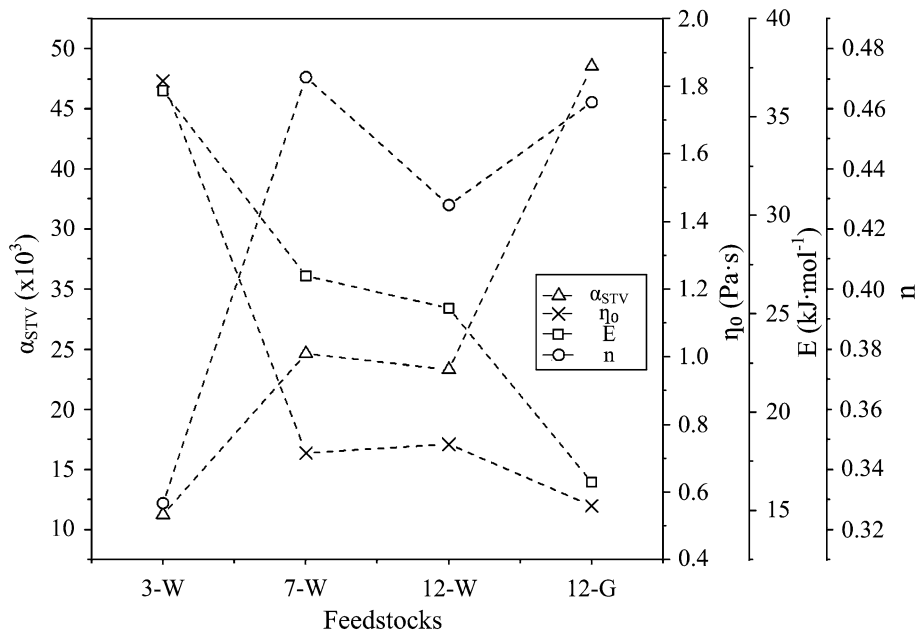
Fig. 6 Moldability index (α_{STV}), reference viscosity at a reference shear rate of $100 \ s^{-1}$ (η_0), activation energy for flow (E), and shear sensitivity index (n) of feedstocks at 90°C

W, 12-W, and 12-G) exhibit values of n ranging from 0.42 to 0.46, which can be considered similar as compared to the $n = 0.32$ obtained with the feedstock 3-W.

In this study, the capacity of the feedstock to be injected into the mold cavity was assessed through the calculation of the moldability index (α_{STV} presented in Eq 2), which is reported in Fig. 6. This model combines the viscosity value with the shear rate and temperature sensitivity to predict the molding capability of feedstocks. From a molding perspective, the best feedstock candidate corresponds to the highest value of α_{STV} which is obtained for the lowest value of η_0, n, and E, concurrently. In this respect, feedstock 12-G demonstrates the best properties for the injection step of the LPIM process, while feedstock 3-W exhibits the least desirable moldability index value (Fig. 6). The α_{STV} values obtained for feedstocks 7-W and 12-W are similar, indicating that a coarser powder (i.e., 12 versus 7 μm) does not have a significant effect on the molding properties during injection. In the absence of an injection problem, the use of finer particles is generally suitable to minimize shrinkage during the sintering step of the process. The sinterability and moldability in this specific particle size distribution range will be studied in future works.

3.4 Segregation Analyses

Thermogravimetric analysis (TGA) was used to measure the weight fraction of the remaining powder after binder burnout at three different positions within the molded specimens (i.e., top, middle, and bottom, according to the pattern shown in Fig. 1c). Figure 7 presents a typical TGA profile obtained with feedstock 12-W, where the binder starts and ultimately burns around 175°C and 400°C, respectively. For convenience, the weight fraction of powder was converted in terms of volume fraction of powder using Eq 3, and then compared to the nominal solid loading set at 60 vol.% in this study.
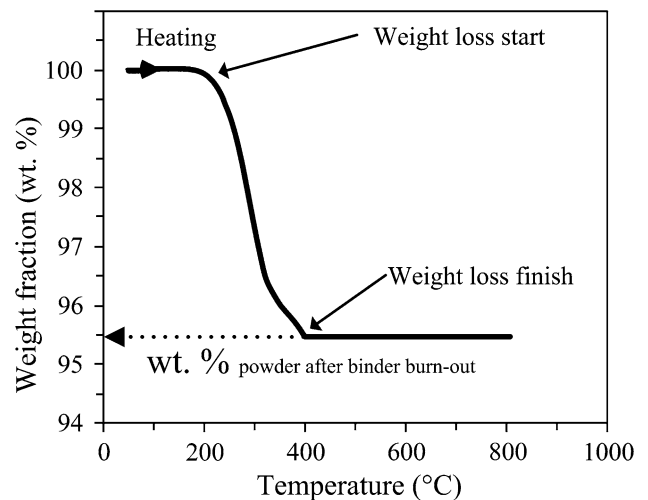

Fig. 7 Typical TGA curve obtained with feedstock 12-W (bottom region of the molded specimen and maintained for 60 min in the molten state; c.f. Fig. 1c)

$$\text{vol.\%}_{\text{powder}} = \left[1 + \left(\frac{\rho_{\text{powder}}}{\rho_{\text{binder}}} \right) \cdot \left(\frac{1}{\text{wt.\%}_{\text{powder}}} - 1 \right) \right]^{-1}$$

$$(\text{Eq } 3)$$

where vol.%$_{\text{powder}}$ is the volume fraction of powder, wt.%$_{\text{powder}}$ is the weight fraction of powder measured from the TGA profile, ρ_{powder} is the density of the powder, and ρ_{binder} is the density of the binder, with these latter values reported in Tables 1 and 3.

Segregation profiles representing the evolution of the volume fraction of powder according to the locations within the molded part are presented in Fig. 8 according to the powder size, powder shape, and time spent in molten state. Our

previous work showed that a measurement sensitivity of about ± 0.25 vol.% can be considered for the detection of a real change in local solid loading using the TGA technique (Ref 34). In other words, all feedstocks exhibiting solid loading values outside the 60.0 ± 0.25 vol.% range can be considered as segregated mixtures. In this respect, all solid loading values above or below 60 vol.% represent a powder-rich or a binder-rich zone, respectively. The nominal solid loading is represented by a dashed line in Fig. 8.

For 1 min spent in molten state, no significant segregation was observed within the molded parts for all feedstocks (i.e., < 0.23 vol.% of powder). This result confirms that the binder formulation is well-adapted for standard injection conditions with all powders used in this study. For 10 min spent in molten state, the magnitude of segregation remains insignificant for feedstock 3-W, while phase separation occurs at the top and bottom positions for the other three feedstocks. The intensity of segregation measured within feedstocks 7-W and 12-W is about 2-4 percentage points (lack/excess of powder), and this value increases up to 10 percentage points in excess of powder for feedstock 12-G (i.e., an important powder-rich zone located at the bottom for feedstock 12-G as compared to feedstocks 7-W and 12-W). Assuming that the driving force underlying this type of powder–binder segregation is gravity, the interparticle friction force is the mechanism opposing this segregation, which will thus be weakened as the powder sphericity increases from feedstocks 12-W to 12-G (i.e., similarly to the viscosity results shown in Fig. 5). The segregation during pouring is assumed negligible since the results obtained after 1 min in the liquid state did not exhibit segregation. For 60 min spent in molten state, the segregation measured within feedstock 3-W

was below 1.4 percentage points (lack/excess of powder). This segregation magnitude is very low, considering that the three other feedstocks exhibit a significant difference in solid loading between the top, the middle, and the bottom regions.

Representative SEM images (Fig. 9) taken at different positions within the green part with feedstocks 3-W and 12-G were used to illustrate the powder/binder distribution at different locations. Figure 9(a)-(c) confirms that fine powder is well-distributed along the molded part. After a long time period in the molten state, the solid loading values (varying from 2 to 10 vol.% of powder) measured in the top region of feedstocks 7-W, 12-W, and 12-G confirm a binder-rich zone in which all powders move down over a distance of about 1.2 mm (visible in Fig. 9d). Conversely, the highest solid loading values (converging to the same upper limit of about 70.2-71.3 vol.% of powder) were obtained with the three coarse powder feedstocks, 7-W, 12-W, and 12-G. In this respect, SEM images taken in the middle and the bottom regions of feedstock 12-G (Fig. 9e, f) illustrate a slight increase in powder loading between these two positions within the molded part. Our previous work showed that this maximum value obtained at the bottom location corresponds to the critical solid loading, where all particles are in contact with each other, and the binder just fills the remaining interstices as shown in Fig. 9(f). From a practical perspective, an ideal feedstock should be easy to mold, generate no segregation after injection, and minimize shrinkage after sintering. On the one hand, feedstock 12-G can be considered the best candidate as it demonstrates the highest moldability properties, a low segregation potential if the mixture is injected within 1 min, and a typical powder size used in metal injection molding, i.e., where shrinkage could be
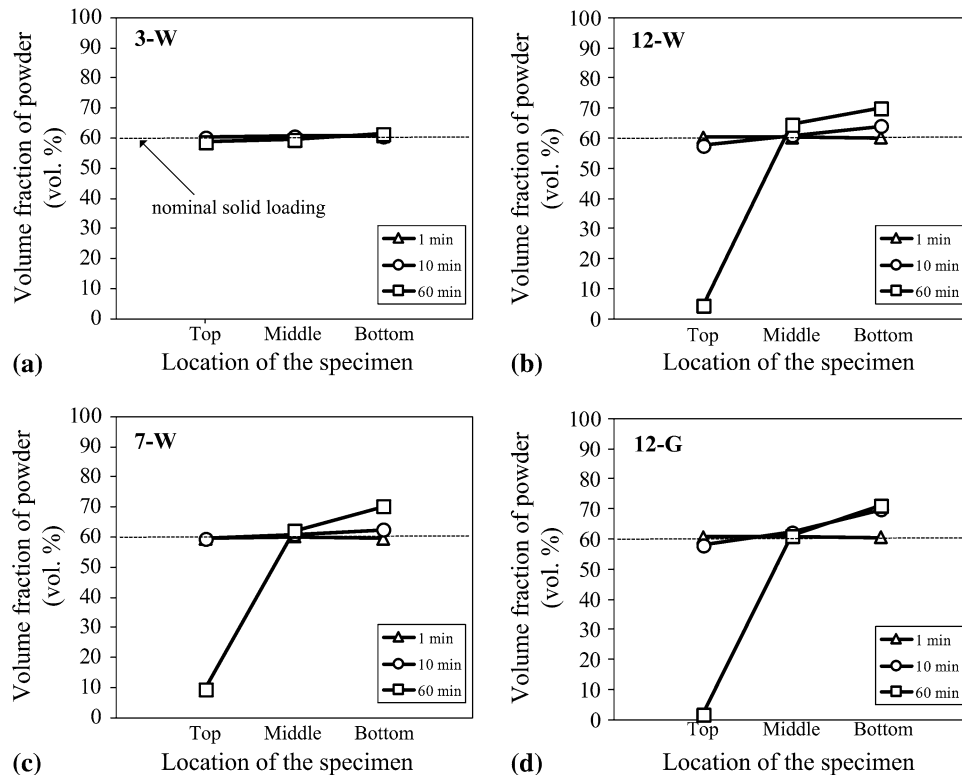

Fig. 8 Volume fraction of powder according to the position, time left in the molten state, and feedstock formulated with (a) water-atomized $D_{50} = 3$ µm, (b) water-atomized $D_{50} = 7$ µm, (c) water-atomized $D_{50} = 12$ µm, and (d) gas-atomized $D_{50} = 12$ µm
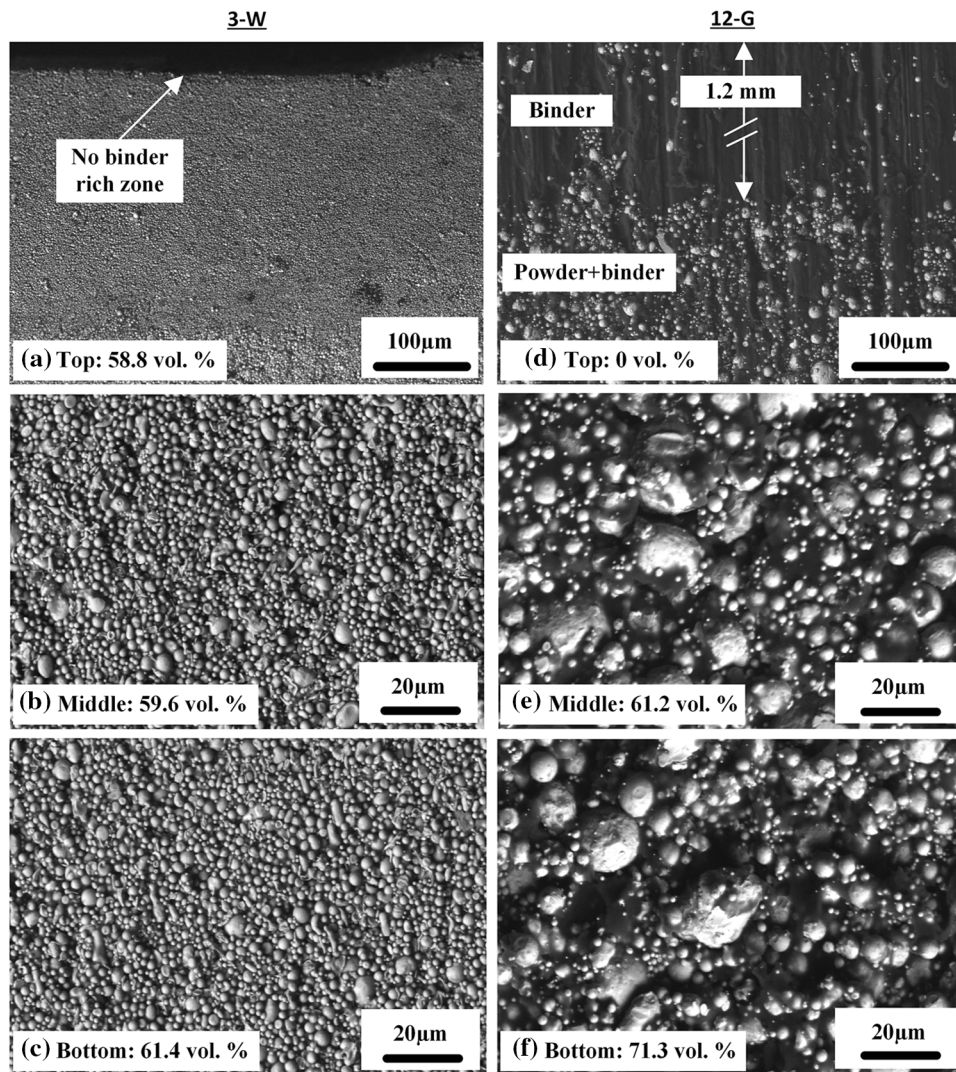
Fig. 9 SEM images (BSE) representing the powder and binder distribution within feedstocks 3-W and 12-G at the top, middle, and bottom locations of the cylinder (60 min spent in molten state)

managed in production. (This latter point was not tested in this work.) On the other hand, the very low segregation potential obtained with feedstock 3-W over any time period spent in molten state could pave the way for future developments of low-viscosity feedstocks (e.g., < 0.1 Pa s) using very-low-viscosity binder to increase moldability, and fine powders to increase sinterability.

4. Conclusion

The influence of particle size and particle shape on rheological, thermal, and segregation properties were investigated for typical 17-4 PH feedstocks used in a low-pressure powder injection molding process. The Weir's model was used to compare the feedstocks and to predict the impact of powder characteristics on the moldability capability of feedstocks.

In contrast to the simple model using a rule of mixture, it was shown that the specific heat capacity is affected by the particle size as well as by the particle shape. As expected, the

lowest and highest viscosity values were obtained with the largest and smallest powder size, respectively. The shear thinning behavior, generally suitable for the LPIM process, was observed over the main shear rate range for all feedstocks, irrespective of the powder size or powder shape because this phenomenon is mainly driven by binder molecules' orientation and ordering with flow. It was also shown that the viscosity value is influenced by the sphericity of powder, with water-atomized powders producing more interparticular friction as compared with gas-atomized powders, which generate higher feedstock viscosity. Segregation results confirm that the binder formulation used in this study was well-adapted for standard injection conditions (i.e., using reduced time spent in molten state) with all powder lots. On the one hand, an increase in time spent in the molten state clearly has a detrimental effect on segregation, particularly for the feedstocks formulated with coarse powders (i.e., 7-W, 12-W, and 12-G). On the other hand, the very low segregation effects measured with feedstock 3-W during any time spent in the molten state pave the way for the future development of a new generation of LPIM feedstocks which are insensitive to segregation.

From an injection perspective, it was shown that the feedstocks formulated with coarser and higher spherical particles (i.e., feedstock 12-G in this project) have a higher moldability potential. However, the similar moldability indexes obtained for feedstocks 7-W and 12-W indicate that a coarser powder (d_{50} = 12 versus 7 μm) does not have a significant effect on the molding properties during injection. Since finer particles are generally suitable at the sintering stage of the process, this combined injection/sintering potential of such mixtures must be confirmed for irregular and spherical particles in future work.

Acknowledgments

References

1. D.F. Heaney, *Handbook of Metal Injection Molding*, 1st ed., Woodhead Publishing, Cambridge, 2012
2. R.M. German and A. Bose, *Injection Molding of Metals and Ceramics*, Metal Powder Industries Federation, New Jersey, 1997
3. B. Hausnerova, *Powder Injection Moulding—An Alternative Processing Method for Automotive Items*, InTech, Rijeka, 2011
4. M. Sardarian, O. Mirzaee, and A. Habibolahzadeh, Influence of Injection Temperature and Pressure on the Properties of Alumina Parts Fabricated by Low Pressure Injection Molding (LPIM), *Ceram. Int.*, 2017, **43**(6), p 4785–4793 (**in English**)
5. B. Hausnerova, B.N. Mukund, and D. Sanetrnik, Rheological Properties of Gas and Water Atomized 17-4PH Stainless Steel MIM Feedstocks: Effect of Powder Shape and Size, *Powder Technol.*, 2017, **312**, p 152–158 (**in English**)
6. M. Aslam, F. Ahmad, P.S.M.B.M. Yusoff, K. Altaf, M.A. Omar, H.P.S. Abdul Khalil, and M.R. Raza, Investigation of Rheological Behavior of Low Pressure Injection Molded Stainless Steel Feedstocks, *Adv. Mater. Sci. Eng.*, 2016, **2016**, p 1–9 (**in English**)
7. R. Ibrahim, M. Azmirruddin, M. Jabir, N. Johari, M. Muhamad, and A.R.A. Talib, Injection Molding of Inconel 718 Parts for Aerospace Application Using Novel Binder System Based on Palm Oil Derivatives, *Int. J. Mech. Aerosp. Ind. Mechatron. Manuf. Eng.*, 2012, **6**, p 2112–2116 (**in English**)
8. J.A. Mangels and R.M. Williams, Injection Molding Ceramics to High Green Densities, *Am. Ceram. Soc. Bull.*, 1983, **62**, p 601–606 (**in English**)
9. K.R. Jamaludin, N. Muhamad, M.N.A. Rahman, S. Murtadhahadi, M.H. Ahmad, and N.H. Nor, Rheological Investigation of Water Atomized Metal Injection Molding (MIM) Feedstock for Processibility Prediction, *Adv. Mater. Res.*, 2010, **83–86**, p 945–952 (**in English**)
10. D.F. Heaney, R. Zauner, C. Binet, K. Cowan, and J. Piemme, Variability of Powder Characteristics and Their Effect on Dimensional Variability of Powder Injection Moulded compoNents, *Powder Metall.*, 2004, **47**, p 145–150 (**in English**)
11. J.M. Contreras, A. Jimenez-Morales, and J.M. Torralba, Experimental and Theoretical Methods for Optimal Solids Loading Calculation in MIM Feedstocks Fabricated from Powders with Different Particle Characteristics, *Powder Metall.*, 2010, **53**, p 34–40 (**in English**)
12. B. Hausnerova, T. Kitano, and P. Saha, Effect of Particle Size Distribution on the Flow Behaviour of Powder Injection Moulding Materials, in *Proceedings of Latest Trends on Engineering Mechanics, Structures, Engineering Geology. 3rd WSEAS International Conference on Engineering Mechanics, Structures, Engineering Geology (EME-SEG 10)*, 2010, Athens, Greece, p 192–194
13. N. Schlechtriemen, R. Knitter, J. Haußelt, and J.R. Binder, Impact of Powder Morphology on Quality of Low-Pressure Injection Moulded Reaction-Bonded Net Shape Oxide Ceramics, *J. Eur. Ceram. Soc.*, 2013, **33**, p 709–715 (**in English**)
14. T. Standring, S. Blackburn, and P. Wilson, Investigation into Paraffin Wax And Ethylene Vinyl Acetate Blends for Use as a Carrier Vehicle in Ceramic Injection Molding, *Polym. Plast. Technol. Eng.*, 2016, **55**, p 802–817 (**in English**)
15. B. Hausnerová, V. Kasparkova, E. Hnátková, Rheological and Thermal Performance of Newly Developed Binder Systems for Ceramic Injection Molding, in *AIP Conference Proceedings of VIII International Conference on "Times of Polymers and Composites": from Aerospace to Nanotechnology*, 2016, p 020120-1–020120-4
16. V. Demers, S. Turenne, and O. Scalzo, Impact of Binders on Viscosity of Low-Pressure Powder Injection Molded Inconel 718 Superalloy, *J. Mater. Sci.*, 2015, **50**, p 2893–2902 (**in English**)
17. M.T. Zaky and N.H. Mohamed, Influence of Low-Density Polyethylene on the Thermal Characteristics and Crystallinity of High Melting Point Macro-And Micro-Crystalline Waxes, *Thermochim. Acta*, 2010, **499**, p 79–84 (**in English**)
18. C. Binet, D.F. Heaney, R. Spina, and L. Tricarico, Experimental and Numerical Analysis of Metal Injection Molded Products, *J. Mater. Process. Technol.*, 2005, **164–165**, p 1160–1166 (**in English**)
19. C.I. Chung, B.J. Carpenter, M.Y. Cao, C.X. Liu, and B.O. Rhee, Property Characterization of Feedstock for Powder Injection Molding, *Adv. Powder Metall.*, 1990, **3**, p 247–282 (**in English**)
20. H. Ishida and S. Rimdusit, Heat Capacity Measurement of Boron Nitride-Filled Polybenzoxazine: The Composite Structure-Insensitive Property, *J. Therm. Anal. Calorim.*, 1999, **58**, p 497–507 (**in English**)
21. L. Kowalski and J. Duszczyk, Specific Heat of Metal Powder-Polymer Feedstock for Powder Injection Molding, *J. Mater. Sci. Lett.*, 1999, **18**, p 1417–1420 (**in English**)
22. K.H. Kate, R.K. Enneti, S.J. Park, R.M. German, and S.V. Atre, Predicting Powder-Polymer Mixture Properties for PIM Design, *Crit. Rev. Solid State Mater. Sci.*, 2014, **39**, p 197–214 (**in English**)
23. Z.Y. Liu, N.H. Loh, S.B. Tor, and K.A. Khor, Characterization of Powder Injection Molding Feedstock, *Mater. Charact.*, 2002, **49**, p 313–320 (**in English**)
24. C.F. Ihle, A. Tamburrino, and P. Vivero, Effect of Sample Manipulation on the Couette Rheometry Of Copper Concentrates, *Powder Technol.*, 2013, **239**, p 78–85 (**in English**)
25. M. Jenni, R. Zauner, J. Stampfl, J. Morris, Quantitative Study of Process and Material Parameters on Flow Behavior and Powder Binder Separation of Feedstocks: Experimental Design 3D Simulation Model and Balance Model for Separation in Suspensions, in *2008 World Congress on Powder Metallurgy and Particulate Materials, PowderMet 2008*, 2018, Washington DC, United states, p 1169–1178
26. M. Jenni, R. Zauner, J. Stampfl, Measurement Methods for Powder Binder Separation in PIM Components, in *Proceedings of EURO PM 2009, European Powder Metallurgy Association (EPMA)*, Copenhagen, Denmark, 2009, p 141–146
27. F. Fareh, V. Demers, S. Turenne, and O. Scalzo, Segregation Measurement of Inconel 718 Feedstocks Used in Low-Pressure Metal Injection Molding, *Mater. Sci. Forum*, 2016, **857**, p 286–290 (**in English**)
28. J.C. Gelin, T. Barriere, and J. Song, Processing Defects and Resulting Mechanical Properties After Metal Injection Molding, *J. Eng. Mater. Technol.*, 2010, **132**, p 011017–0110179 (**in English**)
29. W. Fang, X. He, R. Zhang, S. Yang, and X. Qu, The Effects of Filling Patterns on the Powder–Binder Separation in Powder Injection Molding, *Powder Technol.*, 2014, **256**, p 367–376 (**in English**)
30. H. Hao, L. Yimin, L. Jia, L. Dapeng, and L. Chen, Prediction of Density Variation in Powder Injection Moulding-Filling Process by Using Granular Modelling with Interstitial Power-Law Fluid, *Powder Technol.*, 2016, **291**, p 52–59 (**in English**)
31. W. Yuhui, Q. Xuanhui, Z. Wangfeng, and L. Yan, Analysis of Powder Segregation in Powder Injection Molding, *Adv. Mater. Res.*, 2011, **217**(1372), p 1379 (**in English**)
32. B. Hausnerová, D. Sanétrník, and P. Ponizil, Surface Structure Analysis of Injection Molded Highly Filled Polymer Melts, *Polym. Compos.*, 2013, **34**, p 1553–1558 (**in English**)
33. B. Hausnerová, D. Sanétrník, Quantitative Analysis of Surface Properties Resulting from Powder-Binder Separation, in *Proceedings of Euro PM 2013, European Powder Metallurgy Association (EPMA)*, Gothenburg, Sweden, 2013

34. V. Demers, F. Fareh, S. Turenne, N. Demarquette, and O. Scalzo, Experimental Study on Moldability and Segregation of Inconel 718 Feedstocks Used in Low-Pressure Powder Injection Molding, *Adv. Powder Technol.*, 2018, **29**, p 180–190 (**in English**)

35. L. Poh, C. Della, S. Ying, C. Goh, and Y. Li, Powder Distribution on Powder Injection Moulding of Ceramic Green Compacts Using Thermogravimetric Analysis and Differential Scanning Calorimetry, *Powder Technol.*, 2018, **328**, p 256–263 (**in English**)

36. T.S. Shivashankar, R.K. Enneti, S.J. Park, R.M. German, and S.V. Atre, The Effects of Material Attributes on Powder–Binder Separation Phenomena in Powder Injection Molding, *Powder Technol.*, 2013, **243**, p 79–84 (**in English**)

37. B.N. Mukund, B. Hausnerová, and T.S. Shivashankar, Development of 17-4PH Stainless Steel Bimodal Powder Injection Molding Feedstock with the help of Interparticle Spacing/Lubricating Liquid Concept, *Powder Technol.*, 2015, **283**, p 24–31 (**in English**)

38. M. Leverkoehne, J. Coronel-Hernandez, R. Dirscherl, I. Gorlov, R. Janssen, and N. Claussen, Novel Binder System Based on Paraffin-Wax for Low-Pressure Injection Molding Of Metal–Ceramic Powder Mixtures, *Adv. Eng. Mater.*, 2001, **3**, p 995–998 (**in English**)

39. I. Majewska-Glabus, L. Zhuang, R. Vetter, and J. Duszczyk, Thermal Debinding of Fe3Al-X Metal Powder Compacts, *J. Mater. Sci.*, 1995, **30**, p 6209–6217 (**in English**)

40. M.A. Omar, The Influence of Stearic Acid on the Properties of Injection Moulding of Stainless Steel Powder, *J. Ind. Technol.*, 2001, **10**(2), p 37–45 (**in English**)

41. ASTM D3418-03 Standard Test Method for Transition Temperatures and Enthalpies of Fusion and Crystallization of Polymers by Differential Scanning Calorimetry

42. ASTM E1269-05 Standard Test Method for Determining Specific Heat Capacity by Differential Scanning Calorimetry

43. F.E. Weir, M.E. Doyle, and D.G. Norton, Moldability of Plastics Based on Melt Rheology, *SPE Trans.*, 1963, **3**, p 32–41 (**in English**)

44. A. Ghanbari, M. Alizadeh, E. Ghasemi, R.Y. Rad, and S. Ghaffari, Preparation of Optimal Feedstock for Low-Pressure Injection Molding of Al/SiC Nanocomposite, *Sci. Eng. Compos. Mater.*, 2015, **22**, p 549–554 (**in English**)

45. J. Hidalgo, A. Jiménez-Morales, and J.M. Torralba, Torque Rheology of Zircon Feedstocks for Powder Injection Moulding, *J. Eur. Ceram. Soc.*, 2012, **32**, p 4063–4072 (**in English**)

46. C. Joon-Phil, L. Hyun-Gon, L. Won-Sik, and L. Jai-Sung, Investigation of the Rheological Behavior of 316L Stainless Steel Micro-Nano Powder Feedstock for Micro Powder Injection Molding, *Powder Technol.*, 2014, **261**, p 201–209 (**in English**)

47. V. Demers, S. Turenne, and O. Scalzo, Segregation Measurement of Powder Injection Molding Feedstock Using Thermogravimetric Analysis, Pycnometer Density and Differential Scanning Calorimetry Techniques, *Adv. Powder Technol.*, 2015, **26**, p 997–1004 (**in English**)

48. L.M. Resende, A.N. Klein, and A.T. Prata, Rheological Properties of Granulometric Mixtures for Powder Injection Molding, *Key Eng. Mater.*, 2001, **189–191**, p 598–603 (**in English**)

49. J.M. Contreras, A. Jimenez-Morales, J.M. Torralba, Influence of Particle Size Distribution and Chemical Composition of the Powder on Final Properties of Inconel 718 Fabricated by Metal Injection Moulding (MIM), in *Proceedings of Euro PM 2009*, *European Powder Metallurgy Association (EPMA)*, 2009, Copenhagen, Denmark

50. C. Joon-Phil, P. Jin-Soo, S. Jun-Il, L. Won-Sik, and L. Jai-Sung, Design of Trimodal Fe Micro-Nanopowder Feedstock for Micro Powder Injection Molding, *Powder Technol.*, 2017, **317**, p 1–5 (**in English**)

51. B. Hausnerová, L. Marcaníková, and P. Filip, Optimization of Powder Injection Molding of Feedstock Based on Aluminum Oxide and Multicomponent Water-Soluble Polymer Binder, *Polym. Eng. Sci.*, 2011, **51**, p 1376–1382 (**in English**)

52. V. Demers, M.M. Elmajdoubi, P. Bocher, Moldability of Low-Pressure Powder Injection Molding Feedstocks, in *World Congress on Powder Metallurgy and Particulate Materials, PowderMet 2017*, 2017, Las Vegas, NV, United States, p 401–414 (**in English**)

Publisher's Note Springer Nature remains neutral with regard to jurisdictional claims in published maps and institutional affiliations.